Mechanical compatibility between $Mg_3(Sb,Bi)_2$ and MgAgSb in thermoelectric modules

Yifan Sun,*,† Jiahui Fu,‡ Yuji Ohishi,‡ Keita Toh,¶ Koichiro Suekuni,¶ Kunihiro Kihou,§ Ushin Anazawa,§ Chul-Ho Lee,§ and Ken Kurosaki*,†

†*Institute for Integrated Radiation and Nuclear Science, Kyoto University, 2, Asashiro-Nishi, Kumatori, Sennan-gun, 590-0494 Osaka, Japan*

‡*Graduate School of Engineering, Osaka University, 2-1 Yamadaoka, Suita, 565-0871, Osaka, Japan*

¶*Department of Applied Science for Electronics and Materials, Interdisciplinary Graduate School of Engineering Sciences, Kyushu University, Kasuga, 816-8580, Fukuoka, Japan*

§*National Institute of Advanced Industrial Science and Technology (AIST), 1-1-1 Umezono, Tsukuba, 305-8568, Ibaraki, Japan*

E-mail: sun.yifan.7r@kyoto-u.ac.jp; kurosaki.ken.6n@kyoto-u.ac.jp

Abstract

Thermoelectric (TE) modules are exposed to temperature gradients and repeated thermal cycles during their operations; therefore, mechanically robust n- and p-type legs are required to ensure their structural integrity. The difference in the coefficients of thermal expansion (CTE) of the two legs of a TE module can cause stress buildup and performance deterioration with frequent thermal cycles. Recently, the n-type Mg_3Sb_2 and p-type MgAgSb have become two promising components of the low-temperature TE modules owing to their high TE performances, non-toxicity and abundance. However, the CTEs of n-Mg_3Sb_2 and p-MgAgSb differ by approximately 10%. Furthermore,

the oxidation resistances of these materials at elevated temperatures are unclear. This work manipulates the thermal expansion of Mg_3Sb_2 by alloying it with Mg_3Bi_2. The addition of Bi to Mg_3Sb_2 reduces the coefficient of linear thermal expansion from 22.6 $\times$ 10^{-6} K^{-1} to 21.2 $\times$ 10^{-6} K^{-1} for $Mg_3Sb_{1.5}Bi_{0.5}$, which is in excellent agreement with that of MgAgSb (21 $\times$ 10^{-6} K^{-1}). Furthermore, thermogravimetric data indicate that both $Mg_3Sb_{1.5}Bi_{0.5}$ and MgAgSb are stable in air and Ar at temperatures below ~570 K. The results suggest the compatibility and robustness of $Mg_3Sb_{1.5}Bi_{0.5}$ and MgAgSb as a pair of thermoelectric legs for low-temperature TE modules.

Keywords

thermoelectric, Mg_3Sb_2, MgAgSb, mechanical properties, thermal expansion, stability

1 Introduction

Globally, it is estimated that approximately 72% of the energy input is lost during operations.[1] The majority of this generated waste heat is low-temperature waste heat ($\leq$573 K),[1–5] which has limited applications and low thermal efficiency.[6,7] Thermoelectric (TE) materials, which use the thermoelectric effect to convert heat into electricity, provide a practical solution to recover waste heat, even at low temperatures. The performance of TE material is determined based on its figure of merit (zT), which is defined as $zT = S^2\sigma T\kappa^{-1}$. Here, S, σ, T, and κ are the Seebeck coefficient ($V\,K^{-1}$), electrical conductivity ($S\,m^{-1}$), absolute temperature (K), and thermal conductivity ($W\,m^{-1}\,K^{-1}$), respectively. Based on the definition of the zT value, an ideal TE material follows the phonon-glass electron-crystal (PGEC) concept, which requires enhanced electrical conductivity but poor thermal conductivity. Over the past few decades, TE materials of various material families, such as Zintl compounds,[8,9] half-Heusler compounds,[10,11] and IV-VI compounds,[12–16] with zT values greater than 1 were discovered. The zT value is a temperature-dependent parameter; therefore, applicability of

the TE material relies on a large zT value in a suitable temperature range. At temperatures less than 473 K, Bi_2Te_3 and Sb_2Te_3 are considered the best TE materials for low-temperature waste-heat harvesting.[17] However, the scarcity of Te limits the mass production of Te-based materials, thereby promoting the search for low-temperature, Te-free TE materials.

Recently fabricated n-type Mg_3Sb_2 using excess Mg[18] and high-purity p-type α-MgAgSb[19] are potentially high-performance replacements for Bi_2Te_3. An outstanding zT value of 1.5 at 716 K was obtained for Mg_3Sb_2[18] by doping with Bi, and a concentration of 20-30 mol% Mg_3Bi_2 ($Mg_3Sb_{1.6}Bi_{0.4}$ to $Mg_3Sb_{1.4}Bi_{0.6}$) was determined optimum for its alloying with Mg_3Sb_2.[20] In addition, n-type Mg_3Sb_2-based single-legs have demonstrated high conversion efficiencies of 10.6% at a temperature difference of 400 K (373-773 K)[21] and 13% at a difference of 495 K (278-773 K),[22] respectively. The zT value of the p-type α-MgAgSb improved significantly owing to the successful fabrication of a high-purity MgAgSb.[19,23,24] A single p-type $MgAg_{0.965}Ni_{0.005}Sb_{0.99}$ leg, soldered with silver contacts, exhibited a device efficiency of 8.5% at a temperature difference of 225 K (293–518 K),[25] outperforming p-type $(Bi,Sb)_2Te_3$-based legs.[26,27] The TE legs with contacts are generally fabricated using a one-step sintering method,[25,28–32] where Ag and Fe contacts are used for MgAgSb[25,29–32] and Mg_3Sb_2-based materials,[28–32] respectively.

In the past two years, Mg_3Sb_2/MgAgSb TE modules were successfully fabricated with excellent conversion efficiencies and stabilities at low temperatures.[30–32] An eight-pair $Mg_3Sb_{1.5}Bi_{0.5}$/MgAgSb TE module demonstrated an efficiency of 7.3% at a hot-side temperature of 593 K.[30] Ying et al.[32] achieved 3% and 8.5% conversion efficiencies using $Mg_3Sb_{0.6}Bi_{1.4}$/MgAgSb at temperature differences of 75 and 260 K, respectively. Although the performance of a TE module is dependent on its zT value, its reliability and longevity depend on the mechanical properties and coefficients of thermal expansion (CTE) of module components, which have not been extensively investigated yet. Ying et al.[31,32] observed a decrease in the efficiency of Mg_3Sb_2/MgAgSb module after extended periods of thermal cycling, attributing to the difference between the CTEs of the n-Mg_3Sb_2 and Fe contact layer. Within the

Mg_3Sb_2/MgAgSb module, the CTE mismatch between the n-type Mg_3Sb_2 and its Fe contact remains the largest. Wu et al.[33] put forward an alloying strategy for selecting contact layers for n-Mg_3Sb_2 and proposed Fe_7Mg_2Cr and Fe_7Mg_2Ti as two candidates with high bonding properties and low contact resistance. However, one must not overlook the importance of matching the CTEs between n-Mg_3Sb_2 and p-MgAgSb because the two legs are much longer than their contact layers. This means that even a small CTE mismatch between the two legs can result in a significant difference in the legs' lengths during thermal cycling. Therefore, manipulation of CTEs of the n- and p-legs is also crucial in minimizing performance deterioration of a TE module over time.

The primary goal of this study is to reduce the thermal expansion mismatch in Mg_3Sb_2/MgAgSb TE module by reducing the thermal expansion of the n-type Mg_3Sb_2. Mg_3Sb_2 was chosen particularly because alloying it with Mg_3Bi_2 over a wide composition range provides room to adjust its CTE while maintaining a high zT value, whereas doping MgAgSb can form impurity phases which are detrimental to its performance. In addition, Mg_3Bi_2 has a lower CTE than that of Mg_3Sb_2;[34,35] therefore, the thermal expansion of $Mg_3Sb_{2-x}Bi_x$ was speculated to vary by changing the composition of the solid-solution.

Herein, we fabricated single-phase $Mg_{3.49}Y_{0.01}Sb_2$,[36] $Mg_{3.49}Y_{0.01}Sb_{1.5}Bi_{0.5}$,[36] and $MgAg_{0.95}Sb$ samples using a melting method. $Mg_{3.5}(Sb,Bi)_2$ was doped with Y to enhance its carrier concentrations and improve its TE properties.[36–38] The samples except for $MgAg_{0.95}Sb$ were compacted by hot-press sintering. The CTEs were evaluated using high-temperature x-ray diffraction (HT-XRD) and dilatometry. In addition, various elastic properties such as Young's modulus, bulk modulus, and Poisson's ratio were determined through pulse-echo sound velocity measurements. A hot-press sintered $MgAg_{0.97}Sb$[39] sample was fabricated for sound velocity measurements. Furthermore, the oxidation resistance and thermal stability of $Mg_{3.5}(Sb,Bi)_2$ and $MgAg_{0.95}Sb$ were investigated using thermogravimetry/differential thermal analysis (TG-DTA). The stability of undoped-$Mg_{3.5}(Sb,Bi)_2$ samples was investigated because minor amounts of dopants such as La, Y, and Te were not expected to affect the

stability of the bulk sample. Finally, the reported data are crucial in designing a mechanically robust Mg_3Sb_2/MgAgSb TE module for low-temperature energy harvesting in future studies.

2 Results and discussion

2.1 Phases and lattice parameters

The XRD patterns of the fabricated $Mg_{3.49}Y_{0.01}Sb_2$, $Mg_{3.49}Y_{0.01}Sb_{1.5}Bi_{0.5}$, and $MgAg_{0.95}Sb$ samples are shown in Figure 1 with reference data.[23,40,41] The diffraction peaks of these investigated samples confirmed the successful preparation of single-phase materials. Impurities such as Ag_3Sb, which could have been generated during the preparation of $MgAg_{0.95}Sb$, were within the detection limit of the XRD apparatus. The lattice parameters of the hexagonal-Mg_3Sb_2 and the tetragonal-MgAgSb phases, listed in Table 1 and 2, are in agreement with the literature.[23,40,42–46] The near-identical lattice parameters of $Mg_{3.49}Y_{0.01}Sb_2$ and Mg_3Sb_2[40] suggest that the excess Mg, used to obtain n-type Mg_3Sb_2, does not affect the lattice parameters of the hexagonal-Mg_3Sb_2 phase.[47] A previous study by Kihou et al.[36] showed that most of the excess Mg used to prepare $(Mg,Y)_3(Sb,Bi)_2$ samples evaporated during synthesis, and some remained in the pores of the prepared samples. Doping Mg_3Sb_2 with Bi increases its lattice parameters due to the larger radius of Bi^{3+} compared to that of Sb^{3+}. Furthermore, as the concentration of Mg_3Bi_2 increases in the Mg_3Sb_2-Mg_3Bi_2 system, the lattice parameters of $Mg_3Sb_{2-x}Bi_x$ solid-solution are well approximated using the Vegard's law, as shown in Figure 2.

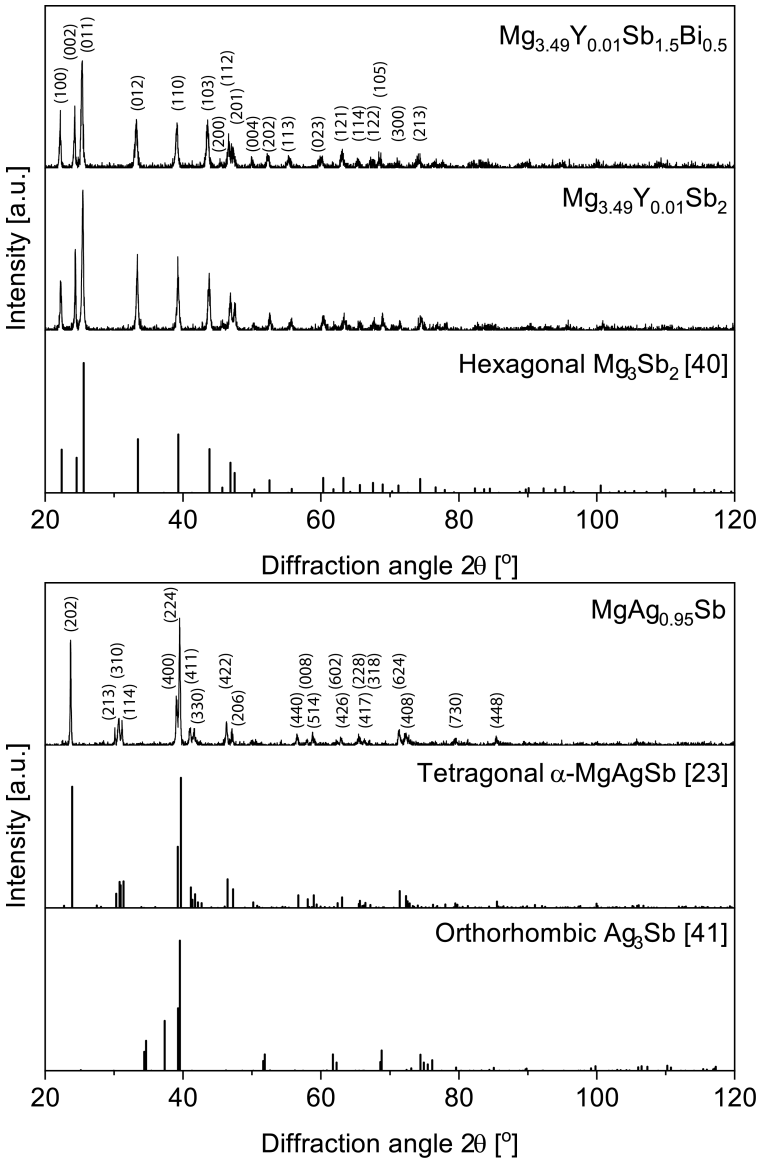

Figure 1: X-ray diffraction patterns (λ=1.54056 Å) of $Mg_{3.49}Y_{0.01}Sb_2$, $Mg_{3.49}Y_{0.01}Sb_{1.5}Bi_{0.5}$, and $MgAg_{0.95}Sb$.

2.2 Thermal expansion

2.2.1 HT-XRD Analysis

The HT-XRD analyses of $Mg_{3.49}Y_{0.01}Sb_2$, $Mg_{3.49}Y_{0.01}Sb_{1.5}Bi_{0.5}$, and $MgAg_{0.95}Sb$ samples were performed under a He environment at temperatures 298–723 K and the patterns are shown in Figures S1, S2, and S3 in the supporting information. Phase transformations are not observed in the HT-XRD patterns of $Mg_{3.49}Y_{0.01}Sb_2$ and $Mg_{3.49}Y_{0.01}Sb_{1.5}Bi_{0.5}$ below 723

Table 1: Lattice parameters of $Mg_{3.49}Y_{0.01}Sb_2$ and $Mg_{3.49}Y_{0.01}Sb_{1.5}Bi_{0.5}$

Sample	a, nm	c, nm	Comment
$Mg_{3.49}Y_{0.01}Sb_2$	0.4559(2)	0.7227(3)	This work
Mg_3Sb_2	0.4568	0.7229	E. Zintl[40]
	0.457	0.725	Zhou et al.[42]
	0.457	0.723	Y. Imai[43]
$Mg_{3.49}Y_{0.01}Sb_{1.5}Bi_{0.5}$	0.4588(7)	0.7286(12)	This work
Mg_3SbBi	0.4608	0.7315	Li et al.[48]
Mg_3Bi_2	0.4666	0.7401	Li et al.[48]
	0.467	0.740	Y. Imai[43]

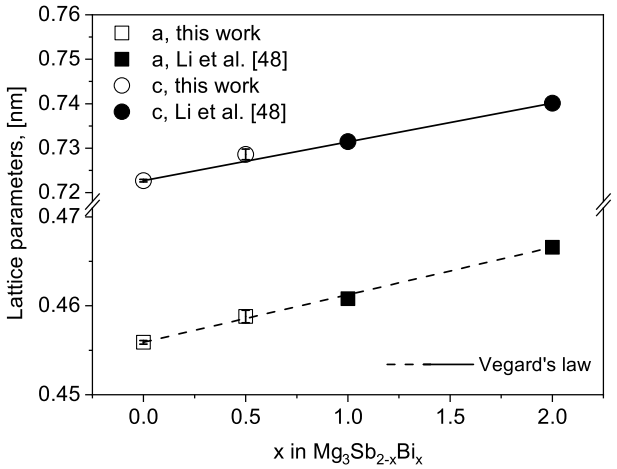

Figure 2: Lattice parameters of $Mg_{3.49}Y_{0.01}Sb_{2-x}Bi_x$ expressed with Vegard's law

Table 2: Lattice parameters of $MgAg_{0.95}Sb$

Sample	a, nm	c, nm	Comment
α-$MgAg_{0.95}Sb$	0.9174(5)	1.2700(14)	This work
α-MgAgSb	0.91761(4)	1.26960(7)	Kirkham et al.[23]
	0.91632(2)	1.2701(1)	Mi et al.[45]
	0.9277	1.2799	Wang et al.[44]
	0.9268	1.2762	N. Miao[46]

K, which is in agreement with previous studies on Mg_3Sb_2.[49,50] The HT-XRD pattern of $MgAg_{0.95}Sb$ demonstrates the $\alpha \rightarrow \beta$ and $\beta \rightarrow \gamma$ phase transitions initiate at 523–573 K and 573–623 K, respectively, which is similar to the phase transition temperatures of ∼563 K and ∼633 K, reported by Kirkham et al.[23] Weak orthorhombic Ag_3Sb impurity peaks are observed at temperature above 673 K, which is the result of a distorted MgAgSb lattice

containing relatively excess Mg or Ag/Sb vacancies and no longer obeying the roughly 1:1:1 stoichiometric ratio.[45]

The temperature-dependent lattice parameters and volumes of each investigated sample are shown in Figure 3, 4, and 5. Error bars represent the standard deviations of the lattice parameters, which are calculated using the Cohen's method.[51] The standard deviations of the lattice volumes are calculated using the law of error propagation. The lattice volumes of $Mg_{3.49}Y_{0.01}Sb_2$ and $Mg_{3.49}Y_{0.01}Sb_{1.5}Bi_{0.5}$ are calculated for a primitive hexagonal unit cell in Figure 3 and 4; the lattice parameters and lattice volumes of the distorted rocksalt-type sublattice of $MgAg_{0.95}Sb$ are shown in Figure 5. The formulas for lattice parameter conversion of MgAgSb were taken from Kirkham et al.[23] The linear line-of-best-fit between the lattice volume and temperature is shown in red, assuming that the coefficient of volumetric thermal expansion (CVTE) is temperature-independent. The corresponding coefficients of linear thermal expansion (CLTEs) and CVTEs of the three materials are listed in Table 3. Large standard errors in the CTEs in this study were due to the limited number of high-quality diffraction peaks at each temperature and HT-XRD measurements (taken every 50 K).

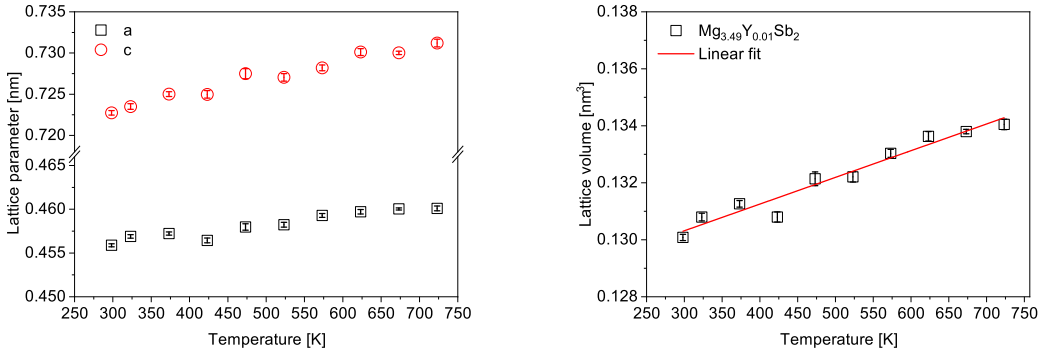

Figure 3: Lattice parameters and lattice volumes of the primitive hexagonal $Mg_{3.49}Y_{0.01}Sb_2$ lattice from 298 to 723 K.

The CLTEs, calculated based on the HT-XRD patterns of $Mg_{3.49}Y_{0.01}Sb_2$ and $MgAg_{0.95}Sb$, are in agreement with literature.[35,52] Peng et al.[52] reported a significantly lower CVTE for

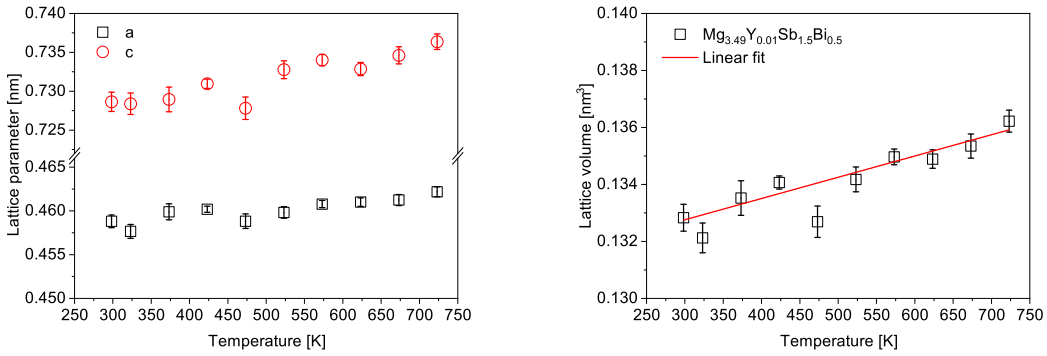

Figure 4: Lattice parameters and lattice volumes of the primitive hexagonal $Mg_{3.49}Y_{0.01}Sb_{1.5}Bi_{0.5}$ lattice from 298 to 723 K.

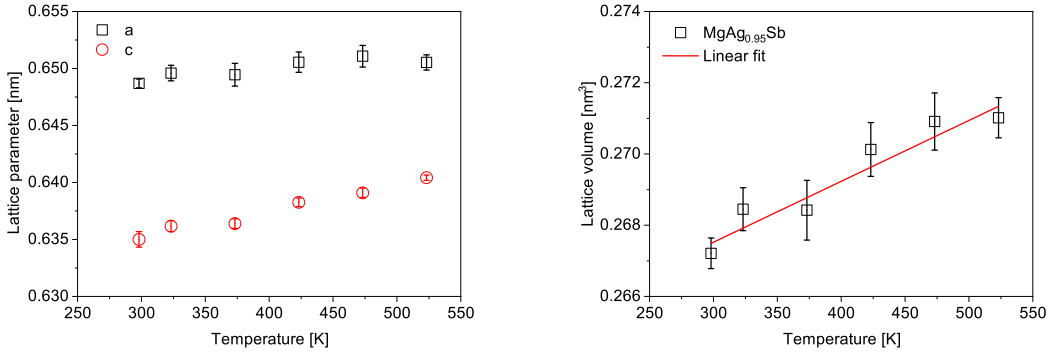

Figure 5: Lattice parameters and volumes of the rocksalt-type sublattice of α-$MgAg_{0.95}Sb$ from 298 to 523 K.

Table 3: Linear (α_L) and volumetric (α_v) thermal expansion coefficients calculated from HT-XRD data with standard error

Sample	Range, K	α_L, 10^{-6} K^{-1}	α_v, 10^{-6} K^{-1}	Comment
$Mg_{3.49}Y_{0.01}Sb_2$	298–723	24.0±1.4	72.0±4.3	HT-XRD + He, this work
Mg_3Sb_2	300–773	22.3	66.9	Dilatometer + He[35]
	-	-	62.7	Calculation[52]
	303–573	-	51.9	HT-XRD + Vacuum[52]
$Mg_{3.49}Y_{0.01}Sb_{1.5}Bi_{0.5}$	298–723	18.7±3.1	56.1±9.2	HT-XRD + He, this work
α-$MgAg_{0.95}Sb$	298–523	21.3±2.7	64.0±8.2	HT-XRD + He, this work
α-MgAgSb	300–573	21	63	HT-XRD + N_2[23]

Mg_3Sb_2 using HT-XRD data. Our HT-XRD results suggest that the addition of Bi to $Mg_{3.49}Y_{0.01}Sb_2$ significantly reduces the CTE of $Mg_{3.49}Y_{0.01}Sb_{1.5}Bi_{0.5}$ to even lower than that of α-$MgAg_{0.95}Sb$. Because the CLTE (α_L) of $Mg_{3.49}Y_{0.01}Sb_{1.5}Bi_{0.5}$ exhibits a large standard

error as only seven low-angle diffraction peaks with high intensity-to-background ratios can be used to calculate its lattice parameter, its CTE was re-evaluated using a dilatometer.

2.2.2 Dilatometry

The thermal expansions of $Mg_{3.49}Y_{0.01}Sb_2$ and $Mg_{3.49}Y_{0.01}Sb_{1.5}Bi_{0.5}$ were measured using a dilatometer at 303–724 K (Figure 6). The corresponding CTEs listed in Table 4 are assumed to be temperature-independent. Standard errors of the CTEs are of the order of 10^{-8} K^{-1}; therefore, they are not included in Table 4. The calculated α_L of $Mg_{3.49}Y_{0.01}Sb_2$ and $Mg_{3.49}Y_{0.01}Sb_{1.5}Bi_{0.5}$ every 50 K are provided in Tables S1 and S2 in the supporting information. The CTE of $Mg_{3.49}Y_{0.01}Sb_2$ was measured to compare with the value reported by Agne et al.[35] The dilatometer data for $Mg_{3.49}Y_{0.01}Sb_2$ exhibits good reproducibility with less than 1.5% deviation from that reported by Agne et al.[35] (Table 4). The CLTE of $Mg_{3.49}Y_{0.01}Sb_{1.5}Bi_{0.5}$, measured using a dilatometer, is slightly higher than that obtained using HT-XRD. Overall, the CTEs obtained using dilatometry are in agreement with literature and depict significantly small standard errors; therefore, the values in Table 4 were used to calculate the mismatch in the thermal expansion coefficients between $Mg_{3.49}Y_{0.01}Sb_{1.5}Bi_{0.5}$ and MgAgSb.

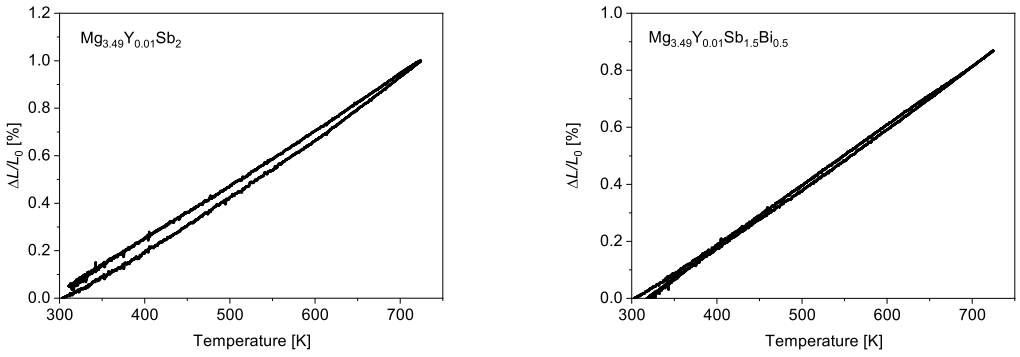

Figure 6: Linear thermal expansion of $Mg_{3.49}Y_{0.01}Sb_2$ and $Mg_{3.49}Y_{0.01}Sb_{1.5}Bi_{0.5}$ from 303 to 724 K measured with dilatometer.

Table 4 demonstrates that doping $Mg_{3.49}Y_{0.01}Sb_2$ with Bi to $Mg_{3.49}Y_{0.01}Sb_{1.5}Bi_{0.5}$ de-

Table 4: Coefficients linear (α_L) and volume (α_v) expansion obtained from the dilatometer. The standard errors are on the order of 10^{-8} K^{-1} and are therefore not included.

Sample	Range, K	α_L, 10^{-6} K^{-1}	α_v, 10^{-6} K^{-1}	Comment
$Mg_{3.49}Y_{0.01}Sb_2$	303–724	22.6	67.8	This work
Mg_3Sb_2	300–773	22.3	66.9	Agne et al.[35]
$Mg_{3.49}Y_{0.01}Sb_{1.5}Bi_{0.5}$	303–724	21.2	63.6	This work

creases CLTE from 22.6 × 10^{-6} K^{-1} to 21.2 × 10^{-6} K^{-1}. Consequently, the difference between the CLTEs of $Mg_{3.49}Y_{0.01}Sb_{1.5}Bi_{0.5}$ and α-MgAgSb (21 × 10^{-6} K^{-1}) reduces to 0.95%, which is significantly lower than those of other n-p leg pairs shown in Table 5. Nearly identical CTEs of the two legs of a TE module, in the case of $Mg_{3.49}Y_{0.01}Sb_{1.5}Bi_{0.5}$ and MgAgSb, result in significantly less thermal stress buildup during the heating/cooling cycles of the module and minimize performance deterioration over time.

Table 5: Linear thermal expansion coefficients α_L of various n-p leg pairs

TE material	α_L, 10^{-6} K^{-1}	Mismatch
n-ZrNiSn[53]	11.0	46.7%
p-ZrCoSb[54]	7.5±0.2	
n-$Mg_2Si_{0.6}Sn_{0.4}$[55]	17	41.7%
p-$MnSi_{1.77}$[55]	12	
n-$Mg_{3.49}Y_{0.01}Sb_{1.5}Bi_{0.5}$[a]	21.2	0.95%
p-MgAgSb[23]	21	

[a] This work.

2.3 Thermal stability and oxidation resistance

2.3.1 Stability under inert atmosphere

Table 6: Thermal stability of $Mg_{3.5}Sb_2$, $Mg_{3.5}Sb_{1.5}Bi_{0.5}$, and $MgAg_{0.95}Sb$ obtained from TG-DTA under inert atmosphere

Sample	Phase change	Mass change
$Mg_{3.5}Sb_2$	Stable at 723 K	No oxidation, no evaporation
$Mg_{3.5}Sb_{1.5}Bi_{0.5}$	Stable at 723 K	No oxidation, slight evaporation
$MgAg_{0.95}Sb$	$\alpha \rightarrow \beta \sim 570$ K	No oxidation, slight evaporation

The TG-DTA diagrams in Figure 7 show no endothermic phase change or exothermic

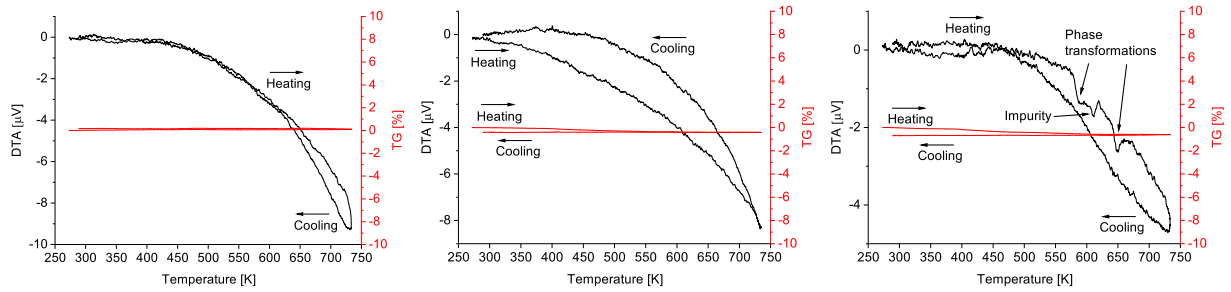

Figure 7: TG-DTA curves of $Mg_{3.5}Sb_2$, $Mg_{3.5}Sb_{1.5}Bi_{0.5}$, and $MgAg_{0.95}Sb$ from 273 to 723 K in Ar

oxidation DTA peaks for $Mg_{3.5}Sb_2$ and $Mg_{3.5}Sb_{1.5}Bi_{0.5}$ below 723 K. Furthermore, mass increases as a result of oxidation is not observed in any investigated samples when heated to 723 K during the TG-DTA analyses (Figure 7). However, $Mg_{3.5}Sb_{1.5}Bi_{0.5}$ and $MgAg_{0.95}Sb$ both exhibit a continuous decrease in mass of approximately 1% with increasing temperature. This decreasing trend is only observed for a short period during initial heating at low temperature, and subsequently stops at high temperatures. While possible excess Mg remaining in $Mg_{3.5}Sb_{1.5}Bi_{0.5}$ after sample preparation could evaporate during TG-DTA experiments, the same reasoning cannot be applied to $MgAg_{0.95}Sb$. Therefore, it is most likely that the mass decrease results from the evaporation of possible contaminants in the platinum crucibles for both materials.

The $\alpha \rightarrow \beta$ and $\beta \rightarrow \gamma$ phase transformations of $MgAg_{0.95}Sb$ completed at approximately 600 and 650 K, respectively. This is in accordance with the HT-XRD results shown in Figure S3 (supporting information) and DSC data reported by Mi et al.[45] The endothermic DTA peak between 600 and 650 K, marked in Figure 7, is speculated to represent the formation of Ag_3Sb impurities detected during HT-XRD measurements. Exothermic DTA peaks, due to the sample oxidation, are absent in the TG-DTA diagram of $MgAg_{0.95}Sb$. During the cooling of $MgAg_{0.95}Sb$, no obvious phase transformations from the γ phase are observed. This is consistent with a previous report by Kirkham et al.,[23] in which a direct and slow transformation of the γ-MgAgSb to α-MgAgSb was noticed during cooling to room temperature. Finally, a summary of the sample's thermal stability when heated to 723 K

under an inert atmosphere is given in Table 6.

2.3.2 Stability in air

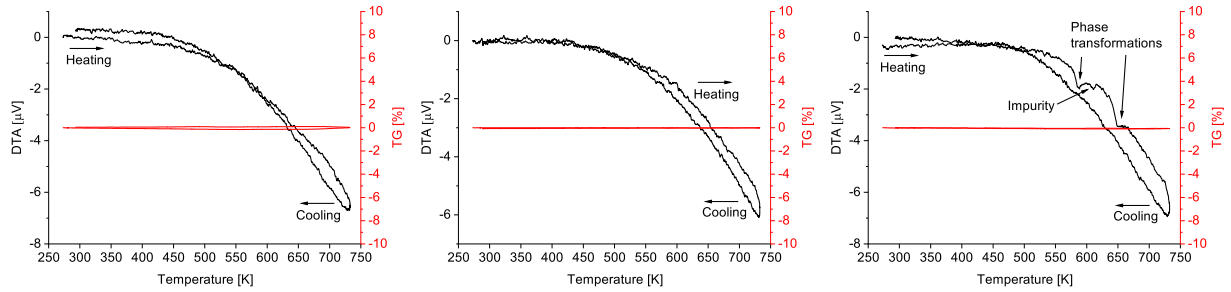

Figure 8: TG-DTA curves of $Mg_{3.5}Sb_2$, $Mg_{3.5}Sb_{1.5}Bi_{0.5}$, and $MgAg_{0.95}Sb$ from 273 to 723 K in air

Table 7: Thermal stability of $Mg_{3.5}Sb_2$, $Mg_{3.5}Sb_{1.5}Bi_{0.5}$, and $MgAg_{0.95}Sb$ obtained from TG-DTA in air

Sample	Phase change	Mass change
$Mg_{3.5}Sb_2$	Stable at 723 K	No oxidation, no evaporation
$Mg_{3.5}Sb_{1.5}Bi_{0.5}$	Stable at 723 K	No oxidation, no evaporation
$MgAg_{0.95}Sb$	$\alpha \rightarrow \beta \sim 570$ K	No oxidation, no evaporation

The TG-DTA diagrams in Figure 8 show no endothermic DTA peaks associated with phase transformations or impurity formation for $Mg_{3.5}Sb_2$ and $Mg_{3.5}Sb_{1.5}Bi_{0.5}$ when the samples are heated up to 723 K in air. Furthermore, the samples do not exhibit a decrease in mass due to evaporation, and no exothermic DTA peaks for oxidation are observed when the samples are heated to 723 K.

Moreover, no significant differences are observed between the HT-XRD patterns of $MgAg_{0.95}Sb$, obtained in He flow and air (supporting information, Figure S3 and S4). The TG-DTA diagram of $MgAg_{0.95}Sb$ indicates that the $\alpha \rightarrow \beta$ and $\beta \rightarrow \gamma$ phase transformations, when heated in air, also finish at approximately 600 and 650 K, respectively. Similarly, the formation of Ag_3Sb is again considered to result in the endothermic DTA peak at slightly higher than 600 K, as shown in the TG-DTA diagram of $MgAg_{0.95}Sb$ in Figure 8. Further, no changes in the sample mass or exothermic DTA peaks resulting from sample oxidation

are observed in $MgAg_{0.95}Sb$ when heated to 723 K in air. Table 7 summarizes the thermal stability of $Mg_{3.5}Sb_2$, $Mg_{3.5}Sb_{1.5}Bi_{0.5}$, and $MgAg_{0.95}Sb$ based on the results obtained from TG-DTA analyses in air. In a previous study, Shang et al.[56] have reported the formation of a high density of pores in $Mg_{3.2}Sb_{0.49}Bi_{1.5}Te_{0.01}$ after measurements at 773 K for 6 hours. Such pore formation was not observed on the surfaces of the $Mg_{3.5}Sb_{1.5}Bi_{0.5}$ samples after TG-DTA experiments in both air and Ar. The SEM images of the $Mg_{3.5}Sb_{1.5}Bi_{0.5}$ samples after TG-DTA measurements are provided in Figure S5 in the supporting information.

2.4 Mechanical properties

2.4.1 Elastic properties

Various elastic properties of $Mg_{3.49}Y_{0.01}Sb_{1.5}Bi_{0.5}$, $Mg_{3.49}Y_{0.01}Sb_2$, and $MgAg_{0.97}Sb$ were calculated from their respective longitudinal and transverse sound velocities using Eq. 2 to 6, and the results are compiled in Table 8. For this measurement, a hot-pressed $MgAg_{0.97}Sb$ sample (98% theoretical density) was used instead of a $MgAg_{0.95}Sb$ ingot obtained by melting, because the pulse-echo measurement failed for the latter despite its high relative density. Overall, doping $Mg_{3.49}Y_{0.01}Sb_2$ with Bi only led to a slight decrease in its Young's modulus to 39.1 GPa, and $Mg_{3.49}Y_{0.01}Sb_{1.5}Bi_{0.5}$ still displays good mechanical compatibility with $MgAg_{0.97}Sb$. This is in agreement with results from previous experimental studies on the elastic properties of $Mg_{3+\delta}Sb_xBi_{2-x}$[57] and MgAgSb.[58] In terms of module design, compatible Young's moduli enhance the module's structural integrity by ensuring that external stress induces similar levels of elastic strain between the n- and p-type legs, which is similar to the concept of matching the thermal expansion between the two legs.

2.4.2 Vickers hardness

Images of the samples, obtained after the Vickers hardness indentation experiments, are shown in Figure S6 in the supporting information. Although Vickers hardness is not a direct measurement of ductility, absence of any cracks along the indentation diagonal sug-

Table 8: Elastic properties of $Mg_{3.49}Y_{0.01}Sb_2$, $Mg_{3.49}Y_{0.01}Sb_{1.5}Bi_{0.5}$, and $MgAg_{0.97}Sb$

	$Mg_{3.49}Y_{0.01}Sb_2$	$Mg_{3.49}Y_{0.01}Sb_{1.5}Bi_{0.5}$	$MgAg_{0.97}Sb$
v_l, $m\,s^{-1}$	3917	3732	3556
v_s, $m\,s^{-1}$	1996	1838	1632
θ_D, K	218	201	194
B, GPa	38.6	40.8	56.5
E, GPa	40.5	39.1	45.2
ν	0.32	0.34	0.37

gests that $Mg_{3.49}Y_{0.01}Sb_2$, $Mg_{3.49}Y_{0.01}Sb_{1.5}Bi_{0.5}$, and $MgAg_{0.95}Sb$ are ductile and do not fracture easily when plastically deformed. The Vickers hardness values of $Mg_{3.49}Y_{0.01}Sb_2$, $Mg_{3.49}Y_{0.01}Sb_{1.5}Bi_{0.5}$, and $MgAg_{0.95}Sb$ are compared with those of other TE materials in Table 9. The uncertainties in the Vickers hardness values, reported in this study, are expressed as standard errors. The Vickers hardness of $MgAg_{0.95}Sb$ is slightly smaller than that reported by Liu et al.[58] with an indentation load of 4.9 N. This difference in the reported Vickers hardness can be attributed to the indentation size effect, considering that this study used a higher load of 9.8 N. Moreover, the MgAgSb fabricated by Liu et al.[58] has a much finer microstructure, which can also result in a higher sample hardness.

Table 9: Vickers hardness of $Mg_{3.49}Y_{0.01}Sb_2$, $Mg_{3.49}Y_{0.01}Sb_{1.5}Bi_{0.5}$, $MgAg_{0.95}Sb$, and other high-performance TE materials

	Vickers hardness, GPa	Comment
$Mg_{3.49}Y_{0.01}Sb_2$	0.62±0.01	This work
$Mg_{3.49}Y_{0.01}Sb_{1.5}Bi_{0.5}$	0.63±0.01	This work
α-$MgAg_{0.95}Sb$	2.26±0.02	This work
α-MgAgSb	2.9	Liu et al.[58]
Mg_2Si	5.4±0.2	Schmidt et al.[59]
$MnSi_{1.77}$	16.0±1.1	Mejri et al.[55]
PbTe	0.37	Ni et al.[60]
Bi_2Te_3	0.62–0.79	G. Guttmann[61]
Zn_4Sb_3	2.2–2.3	G. Guttmann[61]

3 Conclusion

The n-type Mg_3Sb_2 and p-type MgAgSb make a promising pair of TE materials for low-temperature energy harvesting. Prior to the production and practical application of these high-performance TE materials, their mechanical properties should be investigated to avoid mechanical failure during operations. One major concern is the difference between the CTEs of the n- and p-types TE materials, which results in stress buildup in the two legs and can potentially lead to fracture.

Herein, effects of Bi doping on the mechanical properties of n-type $Mg_{3.49}Y_{0.01}Sb_2$ was investigated. The CLTE of $Mg_{3.49}Y_{0.01}Sb_2$ was determined as 22.6 $\times 10^{-6}$ K^{-1}, which is 7.6% higher than that of MgAgSb. The thermal expansion of $Mg_{3.49}Y_{0.01}Sb_2$ was successfully reduced by adding Bi, which is also known to improve its zT value by reducing its thermal conductivity. $Mg_{3.49}Y_{0.01}Sb_{1.5}Bi_{0.5}$ exhibited a CLTE of 21.2 $\times 10^{-6}$ K^{-1}, which significantly reduced the mismatch in the thermal expansion coefficients from 7.6% to 0.95%. In addition, the thermal stabilities and oxidation resistances of $Mg_{3.5}Sb_2$, $Mg_{3.5}Sb_{1.5}Bi_{0.5}$, and $MgAg_{0.95}Sb$ were investigated using TG-DTA. $Mg_{3.5}Sb_2$ and $Mg_{3.5}Sb_{1.5}Bi_{0.5}$ did not show signs of oxidation or evaporation when heated to 723 K in air, and no phase transformation was observed below 723 K. Furthermore, the α-$MgAg_{0.95}Sb$ initiates its $\alpha \rightarrow \beta$ phase transformation at approximately 570 K and did not exhibit sample evaporation or oxidation below 723 K. Calculated elastic properties and Vickers hardness show that $Mg_{3.49}Y_{0.01}Sb_{1.5}Bi_{0.5}$ and $MgAg_{0.97}Sb$ have similar Young's modulus, while $MgAg_{0.97}Sb$ is more resistant to permanent deformation.

Finally, a difference of only 0.95% in the CLTEs of n-type $Mg_{3.49}Y_{0.01}Sb_{1.5}Bi_{0.5}$ and p-type MgAgSb, reliable phase stability, and excellent oxidation resistance in air at temperatures below $\sim$570 K suggest the mechanical robustness of $Mg_{3.49}Y_{0.01}Sb_{1.5}Bi_{0.5}$ and MgAgSb as a pair of n-p legs for low-temperature energy-harvesting TE modules.

4 Experimental Section

4.1 Sample preparation

Polycrystalline samples of both $(Mg,Y)_{3.5}(Sb,Bi)_2$ [36] and $MgAg_{0.95}Sb$ were synthesized using a melting method. The raw materials of Mg, Ag, Sb, Bi, and Y were loaded in an alumina crucible and sealed in a stainless-steel container under an Ar atmosphere. The container was heated up to 1453 and 1273 K for $(Mg,Y)_{3.5}(Sb,Bi)_2$ and $MgAg_{0.95}Sb$, respectively. The obtained molten boule of $(Mg,Y)_{3.5}(Sb,Bi)_2$ was ground and hot-pressed at 873 K under Ar gas flow by applying a uniaxial pressure of 70 MPa. In contrast, grinding and hot pressing were not performed on the molten boule of $MgAg_{0.95}Sb$. The $MgAg_{0.97}Sb$ sample was obtained by melting the constituent elements, followed by ball milling and hot-press sintering.[39] The x-ray powder diffraction pattern of the hot-pressed $MgAg_{0.97}Sb$ sample is provided in the supporting information (Figure S7). Each sample's density is provided in Table 10.

Table 10: Fabricated sample's density

	$Mg_{3.49}Y_{0.01}Sb_2$	$Mg_{3.49}Y_{0.01}Sb_{1.5}Bi_{0.5}$	$MgAg_{0.97}Sb$	$MgAg_{0.95}Sb$
Density, $g\,cm^{-3}$	3.84	4.33	6.21	5.85

4.2 X-ray diffraction

X-ray diffraction experiments were performed at $2\theta = 20°$–$120°$ with CuKα radiation (Ultima IV, Rigaku). Focusing beam HT-XRD experiments were performed under a He atmosphere with the Reactor X HT-XRD attachment. NIST silicon powder was used for angle calibrations, and peaks search was done using the PDXL software by Rigaku, with the sigma cut-off value set to 3.0. Finally, the lattice parameters were calculated using the Cohen's method.[51]

4.3 Dilatometry

The thermal expansions of the hot-pressed samples were measured using a dilatometer (TD5000SA, Bruker AXS) under Ar flow (0.1 L min^{-1}, 6 N, Air Liquide). The heating rate was set to 5 K min^{-1}, and a standard alumina sample was measured simultaneously to cancel the effect of the pushrod's thermal expansion. The coefficient of linear thermal expansion (CLTE, α_L), was calculated using the least-square fit method via following equation:

$$\frac{L - L_0}{L_0} = \alpha_L (T - T_0) \tag{1}$$

where L is the sample length, L_0 is the sample length at 303 K, T is the sample temperature, T_0 is the initial temperature of 303 K. For isotropic materials with small linear thermal expansions, the coefficient of volumetric thermal expansion (CVTE, α_v) was calculated using $\alpha_v = 3\alpha_L$.

4.4 TG-DTA

Thermogravimetric experiments were conducted for the bulk samples using a Bruker TG-DTA2000SA apparatus in both air (20%O_2-80%N_2, Masscoal) and Ar flow (6 N, Air Liquide) to study the oxidation/evaporation behaviors and phase transformations. The heating rate and gas flow rate were set to 10 K min^{-1} and 0.2 L min^{-1}, respectively, for all samples. Bulk samples of approximately 10 mg were used for TG-DTA, and empty Pt crucibles were used for blank runs before each measurement.

4.5 Sound velocity and elastic properties

Various elastic properties were calculated based on the sound velocity of the samples. The longitudinal and transverse sound velocities were measured using a pulse-echo sound velocity measurement system (Echometer 1062, Nihon Matech) at a transducer frequency of 5 MHz. The shear modulus G (GPa), Young's modulus E (GPa), bulk modulus B (GPa), Poisson's

ratio ν, and Debye temperature θ_D (K) were calculated using the following equations:

$$G = \rho v_s^2 \tag{2}$$

$$E = G(\frac{3v_l^2 - 4v_s^2}{v_l^2 - v_s^2}) \tag{3}$$

$$B = \rho(v_l^2 - \frac{4}{3}v_s^2) \tag{4}$$

$$\nu = \frac{1}{2}\frac{v_l^2 - 2v_s^2}{v_l^2 - v_s^2} \tag{5}$$

$$\theta_D = (\frac{h}{k_B})[\frac{9\rho n N_A}{4\pi M(2v_s^{-3} + v_l^{-3})}]^{\frac{1}{3}} \tag{6}$$

ρ, v_s, v_l, h, k_B, n, N_A, and M are the density, transverse sound velocity, longitudinal sound velocity, Planck's constant, Boltzmann's constant, number of atoms per molecule, Avogadro number, and molar mass, respectively.

4.6 Vickers hardness

Vickers hardness measurements were performed using a Vickers Hardness Tester (HMV G-20, Shimadzu) with an applied load of 9.8 N and a hold time of 10 s. Ten measurements were taken for each sample to calculate the average Vickers hardness and assess its uncertainty. The sample's Vickers hardness H_v, was calculated using the equation $H_v = 1.854F/d^2$, where F (kgf) and d (mm) are the applied load and diagonal length, respectively.

Supporting Information Available

Supporting Information: High-temperature XRD diffraction patterns for all samples, coefficients of linear thermal expansion of $Mg_{3.49}Y_{0.01}Sb_2$ and $Mg_{3.49}Y_{0.01}Sb_{1.5}Bi_{0.5}$, SEM images of $Mg_{3.5}Sb_{1.5}Bi_{0.5}$ after TG-DTA, Vickers hardness indentation images, and room-temperature XRD diffraction pattern for $MgAg_{0.97}Sb$ (PDF)

Data Availability Statement

The data are available from the corresponding authors upon reasonable request.

Acknowledgement

This work was supported in part by CREST (No. JPMJCR20Q4) from the Japan Science and Technology Agency, and MEXT/JSPS KAKENHI, (Grant No. JP20K21162).

References

(1) Forman, C.; Muritala, I. K.; Pardemann, R.; Meyer, B. Estimating the Global Waste Heat Potential. *Renewable Sustainable Energy Rev.* **2016**, *57*, 1568–1579.

(2) Johnson, I.; Choate, W. T.; Davidson, A. *Waste Heat Recovery: Technology and Opportunities in US Industry*; 2008; p 10.

(3) Lu, H.; Price, L.; Zhang, Q. Capturing the Invisible Resource: Analysis of Waste Heat Potential in Chinese Industry. *Appl. Energy* **2016**, *161*, 497–511.

(4) Papapetrou, M.; Kosmadakis, G.; Cipollina, A.; La Commare, U.; Micale, G. Industrial Waste Heat: Estimation of the Technically Available Resource in the EU per Industrial Sector, Temperature Level and Country. *Appl. Therm. Eng.* **2018**, *138*, 207–216.

(5) Firth, A.; Zhang, B.; Yang, A. Quantification of Global Waste Heat and Its Environmental Effects. *Appl. Energy* **2019**, *235*, 1314–1334.

(6) Xu, Z.; Wang, R.; Yang, C. Perspectives for Low-Temperature Waste Heat Recovery. *Energy* **2019**, *176*, 1037–1043.

(7) Loni, R.; Najafi, G.; Bellos, E.; Rajaee, F.; Said, Z.; Mazlan, M. A Review of Industrial Waste Heat Recovery System for Power Generation With Organic Rankine Cycle: Recent Challenges and Future Outlook. *J. Clean. Prod.* **2021**, *287*, 125070.

(8) Snyder, G. J.; Christensen, M.; Nishibori, E.; Caillat, T.; Iversen, B. B. Disordered Zinc in Zn_4Sb_3 With Phonon-Glass and Electron-Crystal Thermoelectric Properties. *Nat. Mater.* **2004**, *3*, 458–463.

(9) Brown, S. R.; Kauzlarich, S. M.; Gascoin, F.; Snyder, G. J. $Yb_{14}MnSb_{11}$: New High Efficiency Thermoelectric Material for Power Generation. *Chem. Mater.* **2006**, *18*, 1873–1877.

(10) Fu, C.; Bai, S.; Liu, Y.; Tang, Y.; Chen, L.; Zhao, X.; Zhu, T. Realizing High Figure of Merit in Heavy-Band p-Type Half-Heusler Thermoelectric Materials. *Nat. Commun.* **2015**, *6*, 8144.

(11) Zhu, H.; Mao, J.; Li, Y.; Sun, J.; Wang, Y.; Zhu, Q.; Li, G.; Song, Q.; Zhou, J.; Fu, Y., et al. Discovery of TaFeSb-Based Half-Heuslers With High Thermoelectric Performance. *Nat. Commun.* **2019**, *10*, 270.

(12) Jiang, B.; Yu, Y.; Cui, J.; Liu, X.; Xie, L.; Liao, J.; Zhang, Q.; Huang, Y.; Ning, S.; Jia, B., et al. High-Entropy-Stabilized Chalcogenides With High Thermoelectric Performance. *Science* **2021**, *371*, 830–834.

(13) Zhao, L.-D.; Lo, S.-H.; Zhang, Y.; Sun, H.; Tan, G.; Uher, C.; Wolverton, C.; Dravid, V. P.; Kanatzidis, M. G. Ultralow Thermal Conductivity and High Thermoelectric Figure of Merit in SnSe Crystals. *Nature* **2014**, *508*, 373–377.

(14) Chang, C.; Wu, M.; He, D.; Pei, Y.; Wu, C.-F.; Wu, X.; Yu, H.; Zhu, F.; Wang, K.; Chen, Y., et al. 3D Charge and 2D Phonon Transports Leading to High Out-of-Plane ZT in n-Type SnSe Crystals. *Science* **2018**, *360*, 778–783.

(15) Hazan, E.; Ben-Yehuda, O.; Madar, N.; Gelbstein, Y. Functional Graded Germanium–Lead Chalcogenide-Based Thermoelectric Module for Renewable Energy Applications. *Adv. Energy Mater.* **2015**, *5*, 1500272.

(16) Tan, G.; Hao, S.; Cai, S.; Bailey, T. P.; Luo, Z.; Hadar, I.; Uher, C.; Dravid, V. P.; Wolverton, C.; Kanatzidis, M. G. All-Scale Hierarchically Structured p-Type PbSe Alloys With High Thermoelectric Performance Enabled by Improved Band Degeneracy. *J. Amer. Chem. Soc.* **2019**, *141*, 4480–4486.

(17) Snyder, G. J.; Toberer, E. S. Complex Thermoelectric Materials. *Nat. Mater.* **2008**, *7*, 105–114.

(18) Tamaki, H.; Sato, H. K.; Kanno, T. Isotropic Conduction Network and Defect Chemistry in $Mg_{3+\delta}Sb_2$-Based Layered Zintl Compounds With High Thermoelectric Performance. *Adv. Mater.* **2016**, *28*, 10182–10187.

(19) Zhao, H.; Sui, J.; Tang, Z.; Lan, Y.; Jie, Q.; Kraemer, D.; McEnaney, K.; Guloy, A.; Chen, G.; Ren, Z. High Thermoelectric Performance of MgAgSb-Based Materials. *Nano Energy* **2014**, *7*, 97–103.

(20) Imasato, K.; Kang, S. D.; Ohno, S.; Snyder, G. J. Band Engineering in Mg_3Sb_2 by Alloying With Mg_3Bi_2 for Enhanced Thermoelectric Performance. *Mater. Horiz.* **2018**, *5*, 59–64.

(21) Zhu, Q.; Song, S.; Zhu, H.; Ren, Z. Realizing High Conversion Efficiency of Mg_3Sb_2-Based Thermoelectric Materials. *J. Power Sources* **2019**, *414*, 393–400.

(22) Wu, X.; Lin, Y.; Han, Z.; Li, H.; Liu, C.; Wang, Y.; Zhang, P.; Zhu, K.; Jiang, F.; Huang, J., et al. Interface and Surface Engineering Realized High Efficiency of 13% and Improved Thermal Stability in $Mg_3Sb_{1.5}Bi_{0.5}$-Based Thermoelectric Generation Devices. *Adv. Energy Mater.* **2022**, 2203039.

(23) Kirkham, M. J.; dos Santos, A. M.; Rawn, C. J.; Lara-Curzio, E.; Sharp, J. W.; Thompson, A. J. Abinitio Determination of Crystal Structures of the Thermoelectric Material MgAgSb. *Phys. Rev. B* **2012**, *85*, 144120.

(24) Ying, P.; Liu, X.; Fu, C.; Yue, X.; Xie, H.; Zhao, X.; Zhang, W.; Zhu, T. High Performance α-MgAgSb Thermoelectric Materials for Low Temperature Power Generation. *Chem. Mater.* **2015**, *27*, 909–913.

(25) Kraemer, D.; Sui, J.; McEnaney, K.; Zhao, H.; Jie, Q.; Ren, Z.; Chen, G. High Thermoelectric Conversion Efficiency of MgAgSb-Based Material With Hot-Pressed Contacts. *Energy Environ. Sci.* **2015**, *8*, 1299–1308.

(26) Hao, F.; Qiu, P.; Tang, Y.; Bai, S.; Xing, T.; Chu, H.-S.; Zhang, Q.; Lu, P.; Zhang, T.; Ren, D., et al. High Efficiency Bi_2Te_3-Based Materials and Devices for Thermoelectric Power Generation Between 100 and 300 °C. *Energy Environ. Sci.* **2016**, *9*, 3120–3127.

(27) Muto, A.; Kraemer, D.; Hao, Q.; Ren, Z.; Chen, G. Thermoelectric Properties and Efficiency Measurements Under Large Temperature Differences. *Rev. Sci. Instrum.* **2009**, *80*, 093901.

(28) Mao, J.; Zhu, H.; Ding, Z.; Liu, Z.; Gamage, G. A.; Chen, G.; Ren, Z. High Thermoelectric Cooling Performance of n-Type Mg_3Bi_2-Based Materials. *Science* **2019**, *365*, 495–498.

(29) Ying, P.; He, R.; Mao, J.; Zhang, Q.; Reith, H.; Sui, J.; Ren, Z.; Nielsch, K.; Schierning, G. Towards Tellurium-Free Thermoelectric Modules for Power Generation from Low-Grade Heat. *Nat. Commun.* **2021**, *12*, 1121.

(30) Liu, Z.; Sato, N.; Gao, W.; Yubuta, K.; Kawamoto, N.; Mitome, M.; Kurashima, K.; Owada, Y.; Nagase, K.; Lee, C. H., et al. Demonstration of Ultrahigh Thermoelectric Efficiency of $\sim$ 7.3% in Mg_3Sb_2/MgAgSb Module for Low-Temperature Energy Harvesting. *Joule* **2021**, *5*, 1196–1208.

(31) Ying, P.; Reith, H.; Nielsch, K.; He, R. Geometrical Optimization and Thermal-Stability Characterization of Te-Free Thermoelectric Modules Based on MgAgSb/$Mg_3(Bi,Sb)_2$. *Small* **2022**, *18*, 2201183.

(32) Ying, P.; Wilkens, L.; Reith, H.; Rodriguez, N. P.; Hong, X.; Lu, Q.; Hess, C.; Nielsch, K.; He, R. A Robust Thermoelectric Module Based on MgAgSb/$Mg_3(Sb,Bi)_2$ With a Conversion Efficiency of 8.5% and a Maximum Cooling of 72 K. *Energy Environ. Sci.* **2022**, *15*, 2557–2566.

(33) Wu, X.; Han, Z.; Zhu, Y.; Deng, B.; Zhu, K.; Liu, C.; Jiang, F.; Liu, W. A General Design Strategy for Thermoelectric Interface Materials in n-Type $Mg_3Sb_{1.5}Bi_{0.5}$ Single Leg Used in TEGs. *Acta Mater.* **2022**, *226*, 117616.

(34) Kayadibi, F.; Günay, S.; Taşseven, Ç. Studying Static, Dynamic and Transport Properties of Mg_3Bi_2. *Acta Phys. Pol. A.* **2015**, *128*, 440–446.

(35) Agne, M. T.; Imasato, K.; Anand, S.; Lee, K.; Bux, S. K.; Zevalkink, A.; Rettie, A. J.; Chung, D. Y.; Kanatzidis, M. G.; Snyder, G. J. Heat Capacity of Mg_3Sb_2, Mg_3Bi_2, and Their Alloys at High Temperature. *Mater. Today Phys.* **2018**, *6*, 83–88.

(36) Kihou, K.; Kunioka, H.; Nishiate, H.; Lee, C. H. Thermoelectric Properties of Yttrium-Doped $Mg_3(Sb,Bi)_2$ Synthesized by Melting Method. *J. Mater. Res. Technol.* **2021**, *10*, 438–444.

(37) Wang, Y.; Zhang, X.; Liu, Y.; Wang, Y.; Liu, H.; Zhang, J. Enhanced Electrical Transport Performance Through Cation Site Doping in Y-Doped $Mg_{3.2}Sb_2$. *J. Materiomics* **2020**, *6*, 216–223.

(38) Shi, X.; Zhao, T.; Zhang, X.; Sun, C.; Chen, Z.; Lin, S.; Li, W.; Gu, H.; Pei, Y. Extraordinary n-Type Mg_3SbBi Thermoelectrics Enabled by Yttrium Doping. *Adv. Mater.* **2019**, *31*, 1903387.

(39) Toh, K.; Suekuni, K.; Hashikuni, K.; Nishiate, H.; Anazawa, U.; Lee, C.-H.; Ohtaki, M. An Effective Synthesis Route for High-Performance α-MgAgSb Thermoelectric Material. *J. Mater. Sci.* **2022**, *57*, 11265–11273.

(40) Zintl, E.; Husemann, E. Bindungsart und Gitterbau binärer Magnesiumverbindungen. *Z. Phys. Chem.* **1933**, *21*, 138–155.

(41) Burkhardt, W.; Schubert, K. On Brass Like Phases With A3 Related Structure. *Z. Metallkd* **1959**, *50*, 442–452.

(42) Zhou, D.; Liu, J.; Xu, S.; Peng, P. Thermal Stability and Elastic Properties of Mg_3Sb_2 and Mg_3Bi_2 Phases From First-Principles Calculations. *Phys. B: Condens. Matter* **2010**, *405*, 2863–2868.

(43) Imai, Y.; Watanabe, A. Electronic Structures of Mg_3Pn_2 (Pn= N, P, As, Sb and Bi) and Ca_3N_2 Calculated by a First-Principle Pseudopotential Method. *J. Mater. Sci.* **2006**, *41*, 2435–2441.

(44) Wang, J.-F.; Fu, X.-N.; Zhang, X.-D.; Wang, J.-T.; Li, X.-D.; Jiang, Z.-Y. Structural, Elastic, Electronic, and Thermodynamic Properties of MgAgSb Investigated by Density Functional Theory. *Chin. Phys. B* **2016**, *25*, 086302.

(45) Mi, J.-L.; Ying, P.-J.; Sist, M.; Reardon, H.; Zhang, P.; Zhu, T.-J.; Zhao, X.-B.; Iversen, B. B. Elaborating the Crystal Structures of MgAgSb Thermoelectric Compound: Polymorphs and Atomic Disorders. *Chem. Mater.* **2017**, *29*, 6378–6388.

(46) Miao, N.; Ghosez, P. Optimization of Thermoelectric Properties of MgAgSb-Based Materials: a First-Principles Investigation. *J. Phys. Chem. C* **2015**, *119*, 14017–14022.

(47) Imasato, K.; Ohno, S.; Kang, S. D.; Snyder, G. J. Improving the Thermoelectric Performance in $Mg_{3+x}Sb_{1.5}Bi_{0.49}Te_{0.01}$ by Reducing Excess Mg. *APL Mater.* **2018**, *6*, 016106.

(48) Li, J.; Zhang, S.; Wang, B.; Liu, S.; Yue, L.; Lu, G.; Zheng, S. Designing High-Performance n-Type Mg_3Sb_2-Based Thermoelectric Materials Through Forming Solid Solutions and Biaxial Strain. *J. Mater. Chem. A* **2018**, *6*, 20454–20462.

(49) Grube, G.; Bornhak, R. Das Zustandsdiagramm Magnesium-Antimon. *Z. Elektrochem. Angew. Phys. Chem.* **1934**, *40*, 140–142.

(50) Barnes, A.; Guo, C.; Howells, W. Fast-Ion Conduction and the Structure of Beta-Mg_3Bi_2. *J. Phys. Condens. Matter* **1994**, *6*, L467.

(51) Cohen, M. Precision Lattice Constants From X-Ray Powder Photographs. *Rev. Sci. Instrum.* **1935**, *6*, 68–74.

(52) Peng, W.; Petretto, G.; Rignanese, G.-M.; Hautier, G.; Zevalkink, A. An Unlikely Route to Low Lattice Thermal Conductivity: Small Atoms in a Simple Layered Structure. *Joule* **2018**, *2*, 1879–1893.

(53) Jung, D.-Y.; Kurosaki, K.; Kim, C.-E.; Muta, H.; Yamanaka, S. Thermal Expansion and Melting Temperature of the Half-Heusler Compounds: MNiSn (M= Ti, Zr, Hf). *J. Alloys Compd* **2010**, *489*, 328–331.

(54) Silpawilawan, W.; Kurosaki, K.; Ohishi, Y.; Muta, H.; Yamanaka, S. FeNbSb p-Type Half-Heusler Compound: Beneficial Thermomechanical Properties and High-Temperature Stability for Thermoelectrics. *J. Mater. Chem. C* **2017**, *5*, 6677–6681.

(55) Mejri, M.; Thimont, Y.; Malard, B.; Estournès, C. Characterization of the Thermo-Mechanical Properties of p-Type ($MnSi_{1.77}$) and n-Type ($Mg_2Si_{0.6}Sn_{0.4}$) Thermoelectric Materials. *Scr. Mater.* **2019**, *172*, 28–32.

(56) Shang, H.; Liang, Z.; Xu, C.; Song, S.; Huang, D.; Gu, H.; Mao, J.; Ren, Z.; Ding, F. n-Type $Mg_3Sb_{2-x}Bi_x$ With Improved Thermal Stability for Thermoelectric Power Generation. *Acta Mater.* **2020**, *201*, 572–579.

(57) Shu, R.; Zhou, Y.; Wang, Q.; Han, Z.; Zhu, Y.; Liu, Y.; Chen, Y.; Gu, M.; Xu, W.; Wang, Y., et al. $Mg_{3+\delta}Sb_xBi_{2-x}$ Family: A Promising Substitute for the State-of-the-Art n-Type Thermoelectric Materials Near Room Temperature. *Adv. Funct. Mater.* **2019**, *29*, 1807235.

(58) Liu, Z.; Gao, W.; Meng, X.; Li, X.; Mao, J.; Wang, Y.; Shuai, J.; Cai, W.; Ren, Z.; Sui, J. Mechanical Properties of Nanostructured Thermoelectric Materials α-MgAgSb. *Scr. Mater.* **2017**, *127*, 72–75.

(59) Schmidt, R. D.; Case, E. D.; Giles, J.; Ni, J. E.; Hogan, T. P. Room-Temperature Mechanical Properties and Slow Crack Growth Behavior of Mg_2Si Thermoelectric Materials. *J. Electron. Mater.* **2012**, *41*, 1210–1216.

(60) Ni, J. E.; Case, E. D.; Khabir, K. N.; Stewart, R. C.; Wu, C.-I.; Hogan, T. P.; Timm, E. J.; Girard, S. N.; Kanatzidis, M. G. Room Temperature Young's Modulus, Shear Modulus, Poisson's Ratio and Hardness of PbTe–PbS Thermoelectric Materials. *Mater. Sci. Eng. B* **2010**, *170*, 58–66.

(61) Guttmann, G. M.; Gelbstein, Y. In *Bringing Thermoelectricity into Reality*; Aranguren, P., Ed.; IntechOpen: Rijeka, Croatia, 2018; Chapter 4.

TOC Graphic

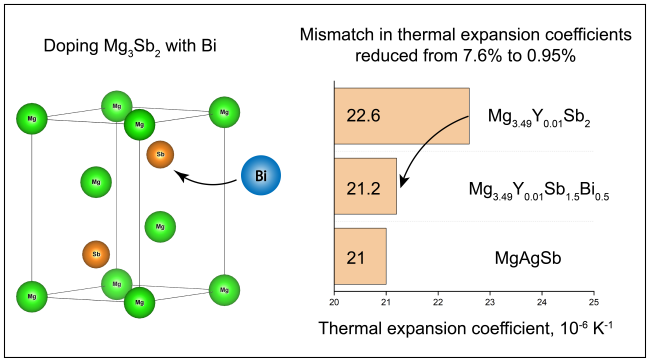
Doping Mg_3Sb_2 with Bi
Mg
Sb
Bi
Mismatch in thermal expansion coefficients reduced from 7.6% to 0.95%
22.6
$Mg_{3.49}Y_{0.01}Sb_2$
21.2
$Mg_{3.49}Y_{0.01}Sb_{1.5}Bi_{0.5}$
21
MgAgSb
20
21
22
23
24
25
Thermal expansion coefficient, 10^{-6} K^{-1}

Mechanical compatibility between $Mg_3(Sb,Bi)_2$ and MgAgSb in thermoelectric modules – Supporting Information

Yifan Sun,[*,†] Jiahui Fu,[‡] Yuji Ohishi,[‡] Keita Toh,[¶] Koichiro Suekuni,[¶] Kunihiro Kihou,[§] Ushin Anazawa,[§] Chul-Ho Lee,[§] and Ken Kurosaki[*,†]

†*Institute for Integrated Radiation and Nuclear Science, Kyoto University, 2, Asashiro-Nishi, Kumatori, Sennan-gun, 590-0494 Osaka, Japan*

‡*Graduate School of Engineering, Osaka University, 2-1 Yamadaoka, Suita, 565-0871, Osaka, Japan*

¶*Department of Applied Science for Electronics and Materials, Interdisciplinary Graduate School of Engineering Sciences, Kyushu University, Kasuga, 816-8580, Fukuoka, Japan*

§*National Institute of Advanced Industrial Science and Technology (AIST), 1-1-1 Umezono, Tsukuba, 305-8568, Ibaraki, Japan*

E-mail: sun.yifan.7r@kyoto-u.ac.jp; kurosaki.ken.6n@kyoto-u.ac.jp

1. High-temperature XRD patterns

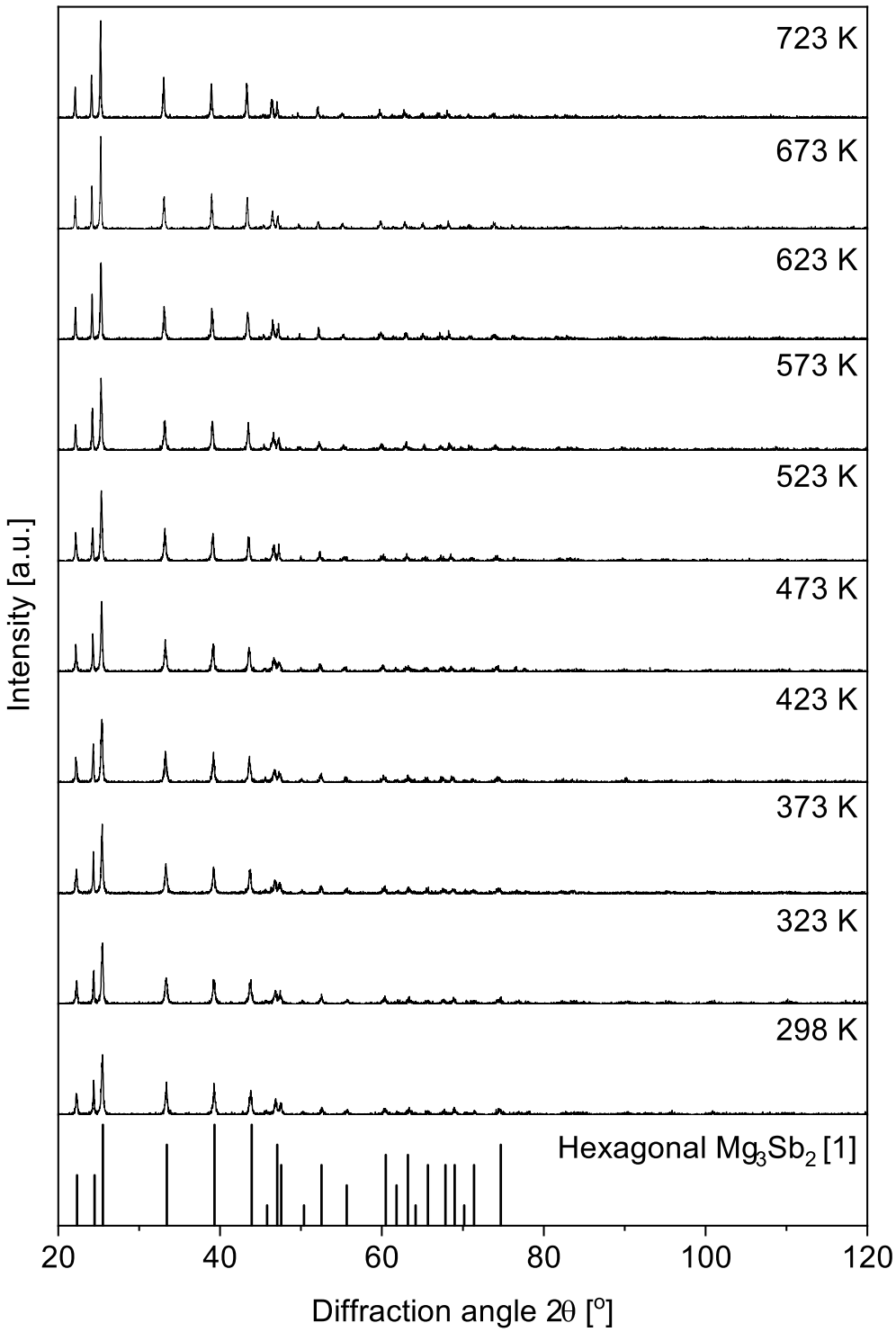

Figure S1: HT-XRD patterns (λ=1.54056 Å) of $Mg_{3.49}Y_{0.01}Sb_2$ from 298 to 723 K in He.

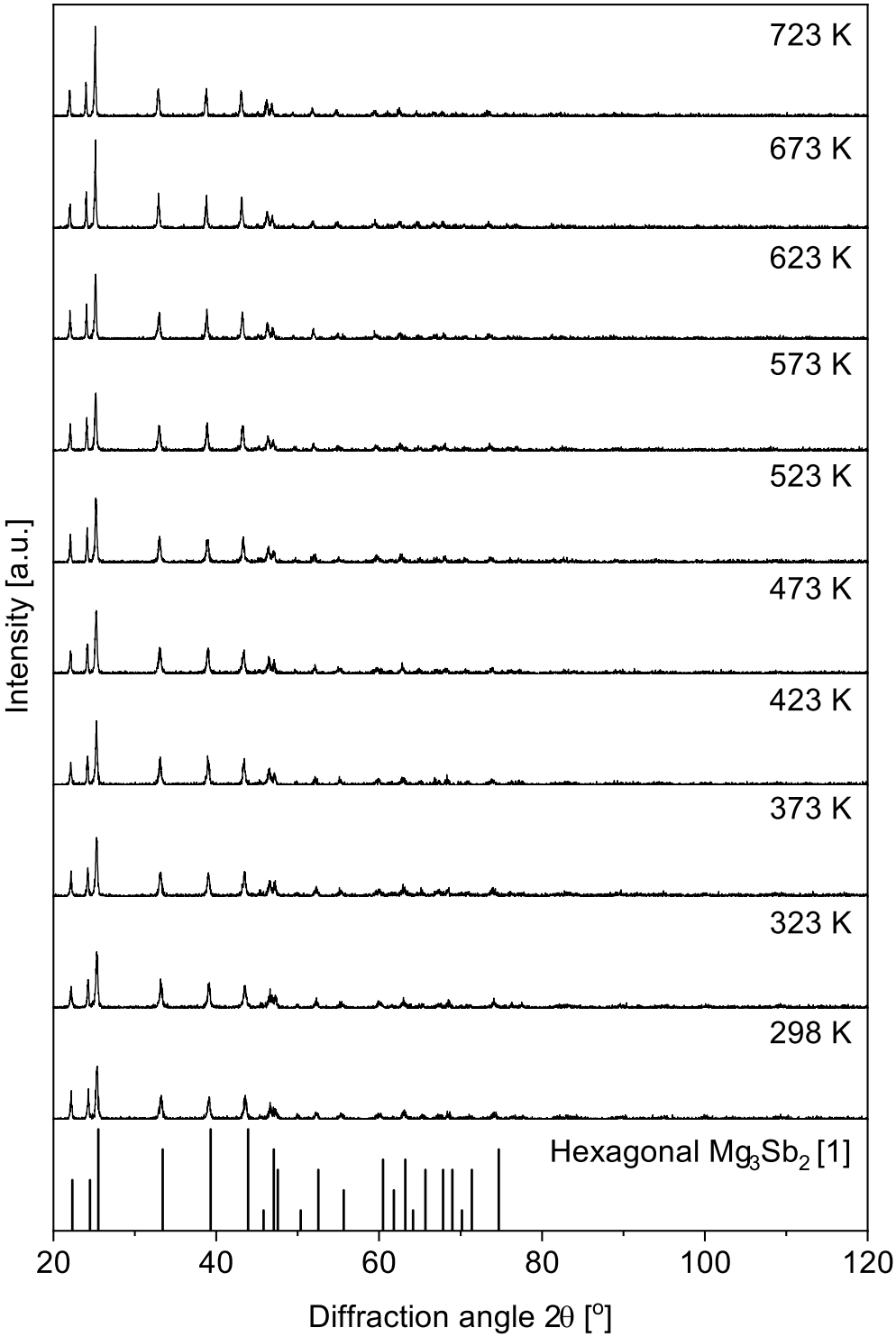

Figure S2: HT-XRD patterns (λ=1.54056 Å) of $Mg_{3.49}Y_{0.01}Sb_{1.5}Bi_{0.5}$ from 298 to 723 K in He.

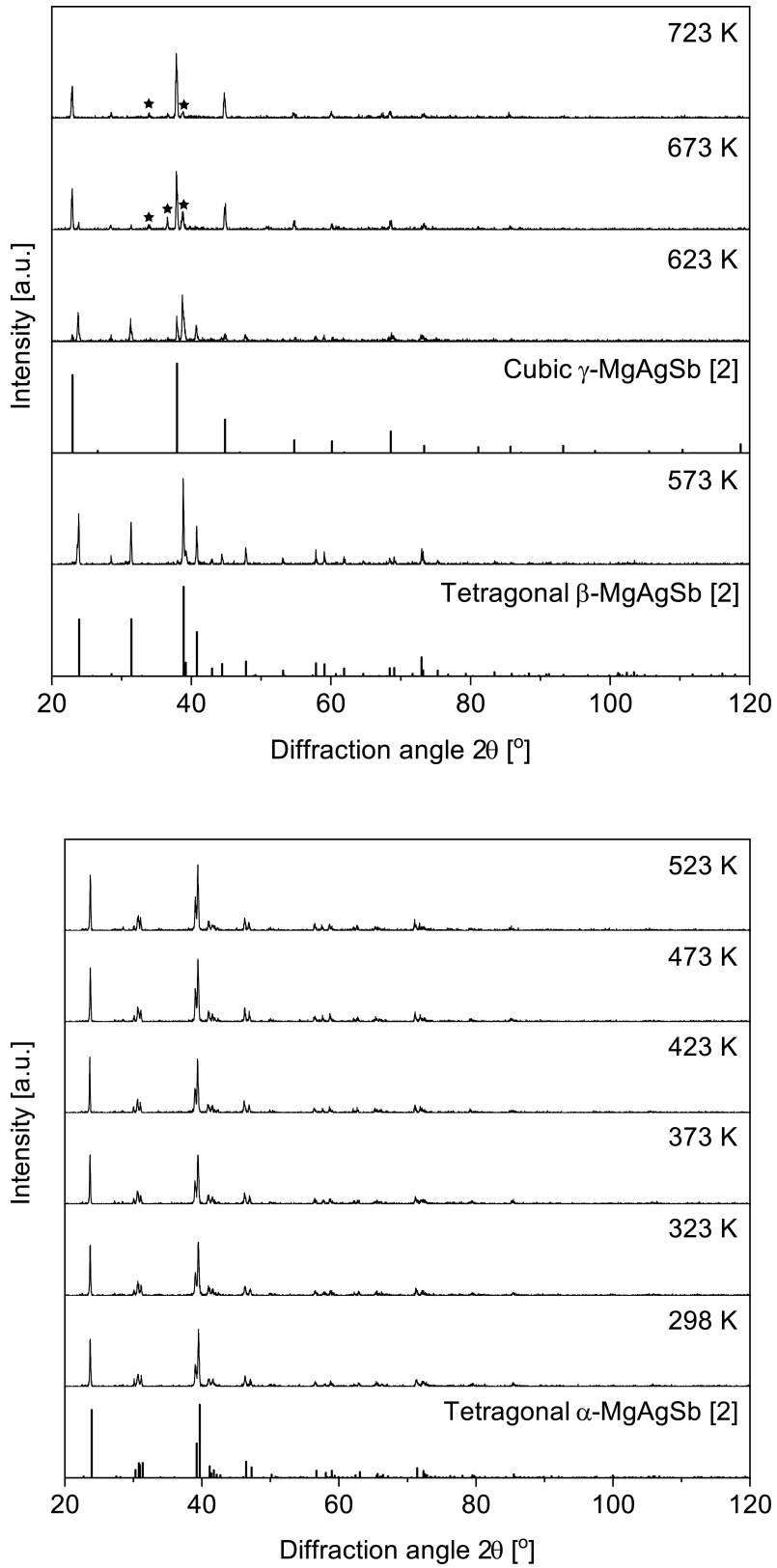

Figure S3: HT-XRD patterns (λ=1.54056 Å) of $MgAg_{0.95}Sb$ from 298 to 723 K in He. Ag_3Sb impurity peaks are marked with $\star$.

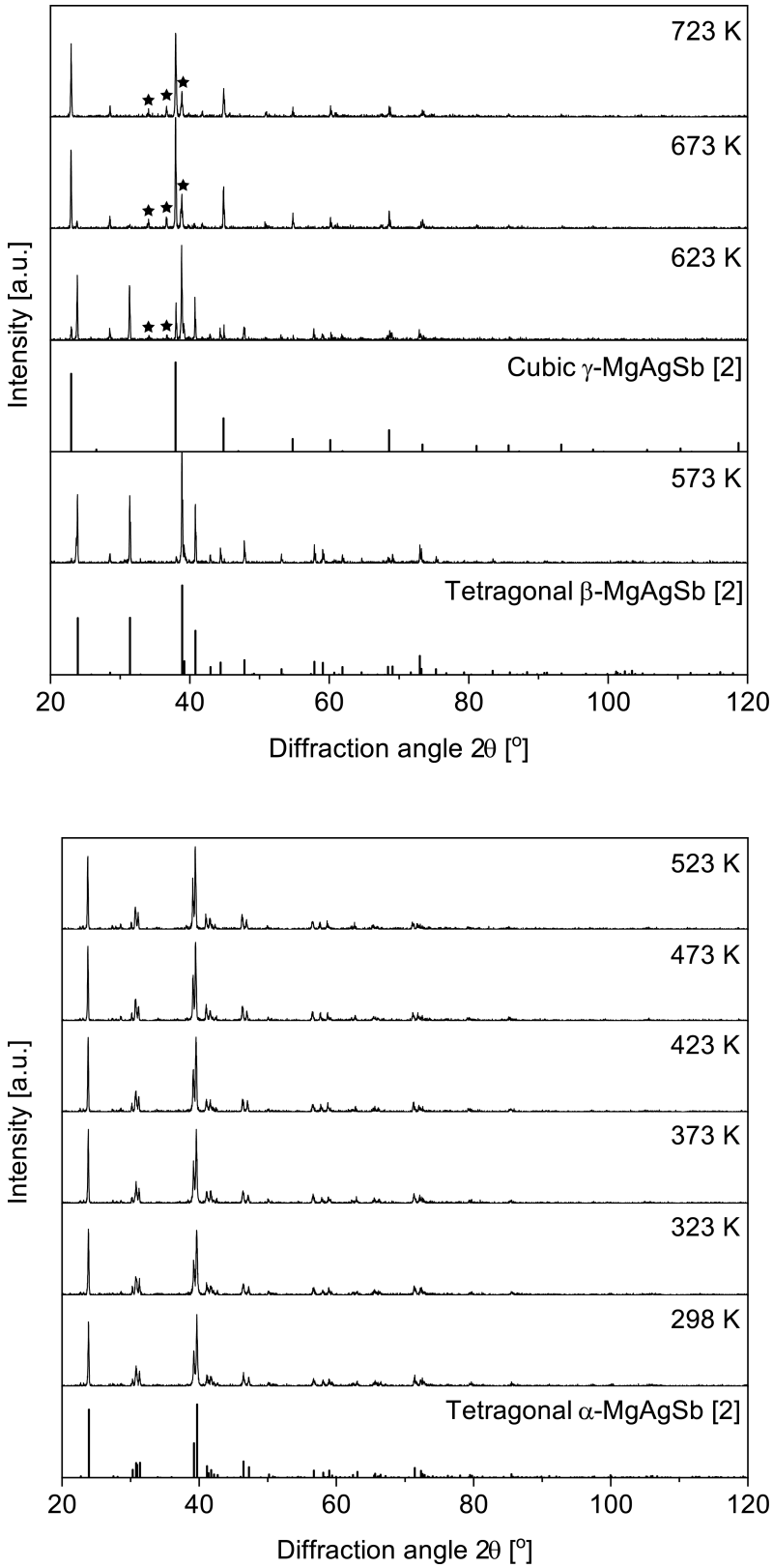

Figure S4: HT-XRD patterns (λ=1.54056 Å) of $MgAg_{0.95}Sb$ from 298 to 723 K in air. Ag_3Sb impurity peaks are marked with $\star$.

2. Linear thermal expansion coefficients of $Mg_{3.49}Y_{0.01}Sb_2$ and $Mg_{3.49}Y_{0.01}Sb_{1.5}Bi_{0.5}$

Table S1: Linear thermal expansion coefficient α_L of $Mg_{3.49}Y_{0.01}Sb_2$, L_0=10.06 mm at 303 K

T, K	$(L-L_0)/L_0$	α_L, 10^{-6} K^{-1}
350	1.10E-3	23.5
400	2.33E-3	24.0
450	3.56E-3	24.2
500	4.27E-3	21.7
550	6.02E-3	24.4
600	7.23E-3	24.3
650	8.41E-3	24.3
700	9.54E-3	24.0
724	9.53E-3	22.6

Table S2: Linear thermal expansion coefficient α_L of $Mg_{3.49}Y_{0.01}Sb_{1.5}Bi_{0.5}$, L_0=14.46 mm at 303 K

T, K	$(L-L_0)/L_0$	α_L, 10^{-6} K^{-1}
350	9.84E-4	20.9
400	2.02E-3	20.8
450	3.05E-3	20.8
500	4.08E-3	20.7
550	5.07E-3	20.5
600	6.15E-3	20.7
650	7.22E-3	20.8
700	8.26E-3	20.8
724	8.94E-3	21.2

3. SEM images of $Mg_{3.5}Sb_{1.5}Bi_{0.5}$ after TG-DTA

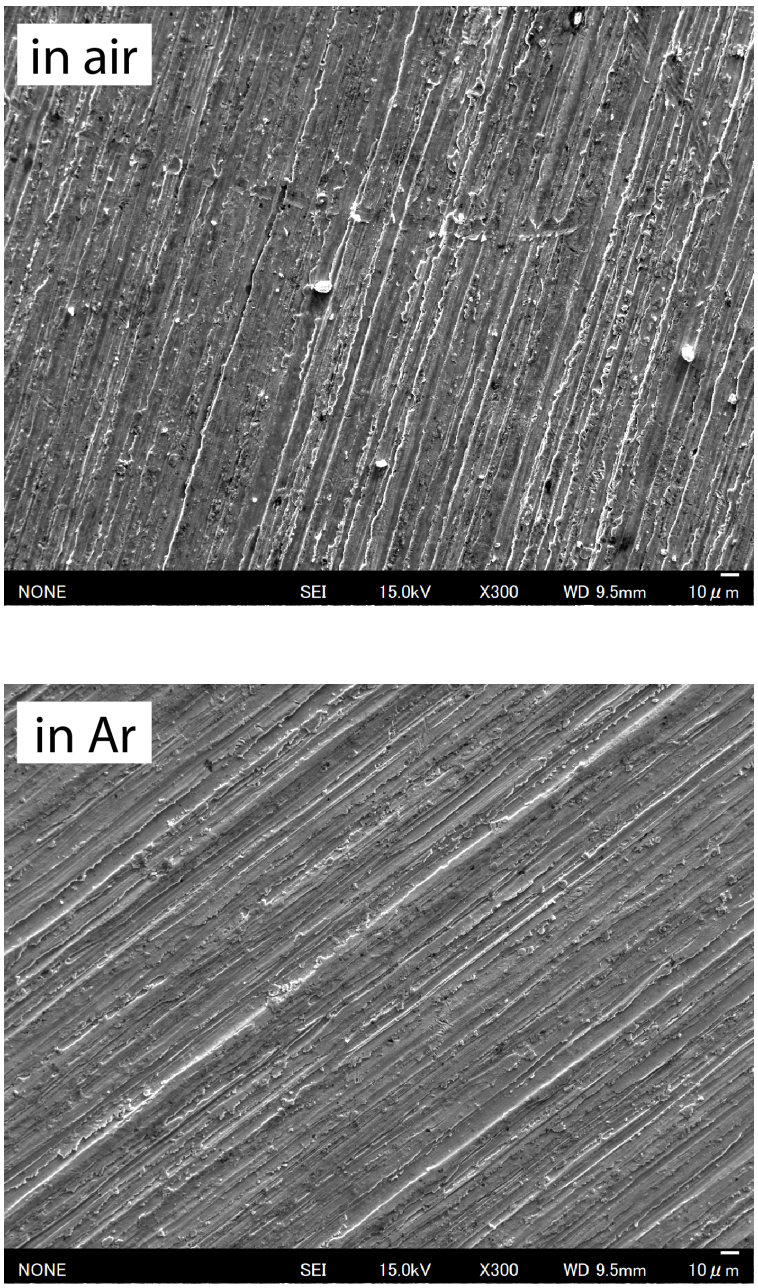

Figure S5: SEM images of the $Mg_{3.5}Sb_{1.5}Bi_{0.5}$ samples after TG-DTA measurements in air and Ar.

4. Vickers hardness indentation

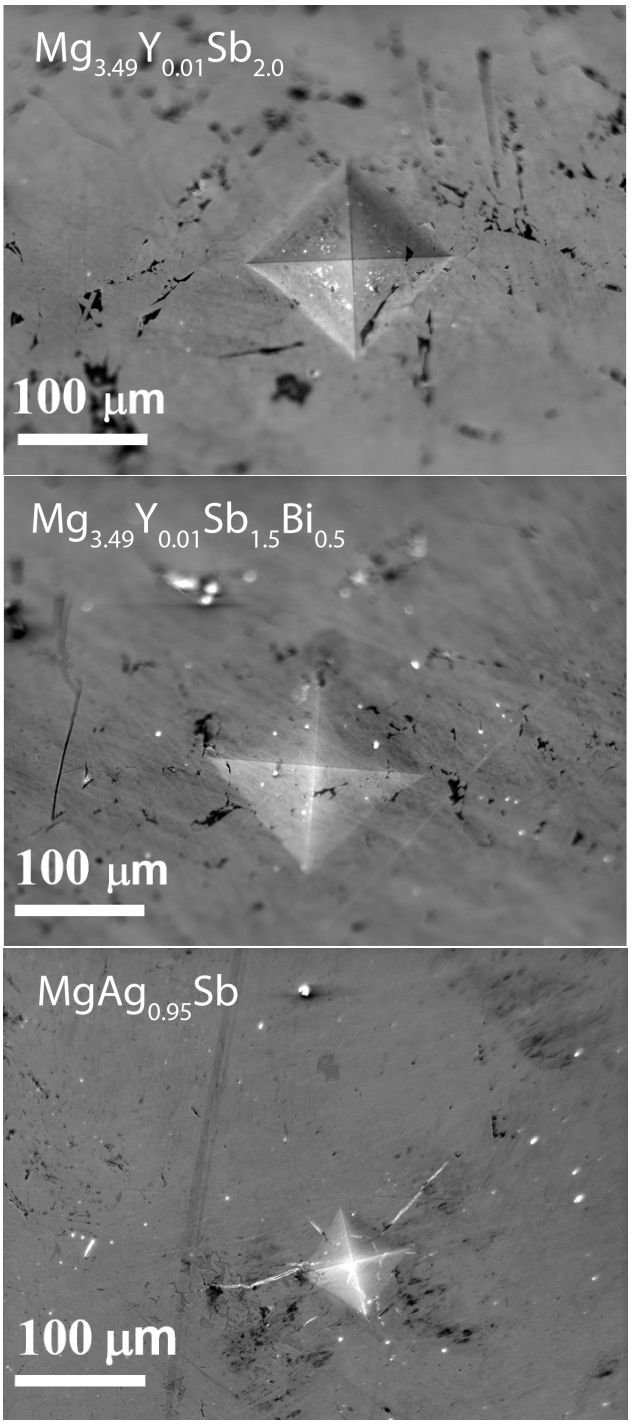

Figure S6: Vickers hardness indentations on $Mg_{3.49}Y_{0.01}Sb_2$, $Mg_{3.49}Y_{0.01}Sb_{1.5}Bi_{0.5}$, and $MgAg_{0.95}Sb$. Small amounts of the excess Mg used to prepare n-type Mg_3Sb_2 are visible in the SEM images of $Mg_{3.49}Y_{0.01}Sb_2$ and $Mg_{3.49}Y_{0.01}Sb_{1.5}Bi_{0.5}$ in black. The white dots are the remains of the alumina polishing fluids.

5. X-ray powder diffraction pattern of $MgAg_{0.97}Sb$

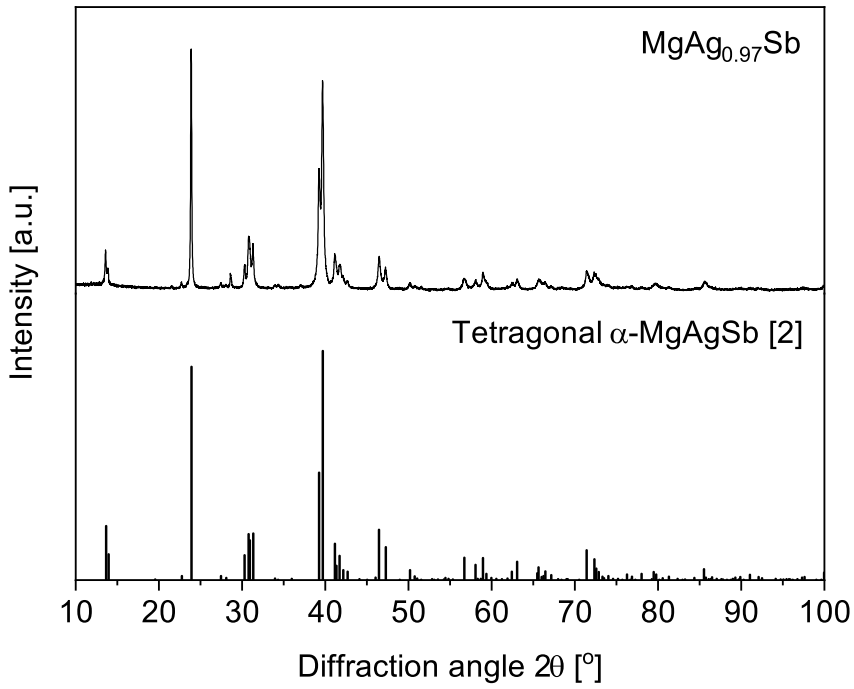

Figure S7: X-ray powder diffraction pattern (λ=1.54056 Å) of $MgAg_{0.97}Sb$.

References

(1) Zintl, E.; Husemann, E. Bindungsart und Gitterbau binärer Magnesiumverbindungen. *Z. Phys. Chem.* **1933**, *21*, 138–155.

(2) Kirkham, M. J.; dos Santos, A. M.; Rawn, C. J.; Lara-Curzio, E.; Sharp, J. W.; Thompson, A. J. Abinitio Determination of Crystal Structures of the Thermoelectric Material MgAgSb. *Phys. Rev. B* **2012**, *85*, 144120.